Received 26 June 2024
Revised 16 August 2024
Accepted 2 September 2024

Fatigue research of metro car body based on operational loads

Xihong Jin and Feng Guo
State Key Laboratory of Heavy-Duty and Express High-Power Electric Locomotive, Product Research and Development Center, CRRC Zhuzhou Locomotive Co., Ltd., Zhuzhou, China

Abstract

Purpose – The principle of infinite life design currently directs fatigue resistance strategies for metro car bodies. However, this principle might not fully account for the dynamic influence of operational loads and the inevitable presence of defects. This study aims to integrate methods of service life estimation and residual life assessment, which are based on operational loads, into the existing infinite life verification framework to further ensure the operational safety of subway trains.

Design/methodology/approach – Operational loads and fatigue loading spectra were determined through the field test. The material test was conducted to investigate characteristics of the fracture toughness and the crack growth rate. The fatigue strength of the metro car body was first verified using the finite element method and Moore–Kommers–Japer diagrams. The service life was then estimated by applying the Miner rule and high-cycle fatigue curves in a modified form of the Basquin equation. Finally, the residual life was assessed utilizing a fracture assessment diagram and a fitted curve of crack growth rate adhered to the Paris formula.

Findings – Neither the maximum utilization factor nor the cumulative damage exceeds the threshold value of 1.0, the metro car body could meet the design life requirement of 30 years or 6.6 million km. However, three out of five fatigue key points were significantly influenced by the operational loads, which indicates that a single fatigue strength verification cannot achieve the infinite life design objective of the metro car body. For a projected design life of 30 years, the tolerance depth is 12.2 mm, which can underscore a relatively robust damage tolerance capability.

Originality/value – The influence of operational loads on fatigue life was presented by the discrepancy analysis between fatigue strength verification results and service life estimation results. The fracture properties of butt-welded joints were tested and used for the damage tolerance assessment. The damage tolerance life can be effectively related by a newly developed equation in this study. It can be a valuable tool to provide the theoretical guidance and technical support for the structural improvements and maintenance decisions of the metro car body.

Keywords Metro car body, Field test, Structural integrity, Damage accumulation, Damage tolerance

Paper type Research paper

1. Introduction

By the end of 2023, 55 cities across China had launched the operation for 306 urban transits, amassing a cumulative mileage exceeding 10,000 km. These subway systems have facilitated impressive 37.6 million train trips, serving astounding 29.4 billion passengers in a single year 2023. These achievements resulted in a considerable number of metro vehicles reaching the mid to late stages of their design life, highlighting an urgent promotion for high-quality development strategies and efficient maintenance decisions.

The authors sincerely appreciate the help provided by the CRRC Zhuzhou Locomotive Co., Ltd. and Shanghai Railway Certification (Group) Co., Ltd. This research was funded by the Major Research Project of CRRC (No. 2022CYY007 and No. 2020CCA094).

Railway Sciences
Vol. 3 No. 5, 2024
pp. 558-574
Emerald Publishing Limited
e-ISSN: 2755-0915
p-ISSN: 2755-0907
DOI 10.1108/RS-06-2024-0023

At present, most of the critical load-bearing components of metro vehicles are generally designed using the infinite life principle, such as wheelsets, bogie frames and the car body. The principle is predicated on two fundamental assumptions (Wu *et al.*, 2021): the load-bearing structures are idealized as free from any inherent flows, and the fatigue loads can be approximated as static or quasi-static constant amplitude loads.

As a large-scale welded component, the metro car body inevitably contains various manufacturing defects and is subject to service damage (Zhou, Wu, Guo, Hu, & Zhang, 2020). As summarized in Figure 1, recent investigations indicated that the stress corrosion and welded imperfections were the principal instigators of the fatigue failure.

Notably, the defect locations marked in Figure 1 are merely used for the illustrative purposes, which do not correspond to the exact positions on any specific metro car bodies. Specifically, Lu, Li, and Shen (2022) revealed a total of 20 fatigue cracks on draft sills of metro car bodies of Guangzhou subway trains after a mere decade of operation. Their findings attributed nine cracks from welded defects, while 11 cracks were attributed to the stress corrosion of Al alloys 7020-T6, with one notable crack reaching a length of 400 mm. Similar investigations detected more than a huge number of 100 cracks on the coupler mounts, anti-roll bar mounts, and reinforcing ribs of the car body for the Shanghai subway trains (Ding, 2023; Wang, 2018); as well as a total of 23 cracks were found on draft-bolster-buffer assemblies of 15 car bodies for the Wuhan metro (Wang & Yuan, 2019).

The rapid development of fracture mechanics and damage tolerance design methods has introduced innovative solutions for the damage tolerance life assessment of railway structures with defects. Guo *et al.* (2021) established a novel time-domain stepwise fatigue assessment framework to bridge the safe life estimation principle with the damage tolerance assessment principle. This innovative methodology has been effectively applied to structural integrity issues, such as the maglev bogie for the high-speed maglev train (Guo *et al.*, 2021, 2022), wheelsets for railway vehicles (Hu, Wu, Xin, Guo, & Ren, 2023) and bogie frames for high-speed trains (Guo, Wu, Liu, Wu, & Zhang, 2023).

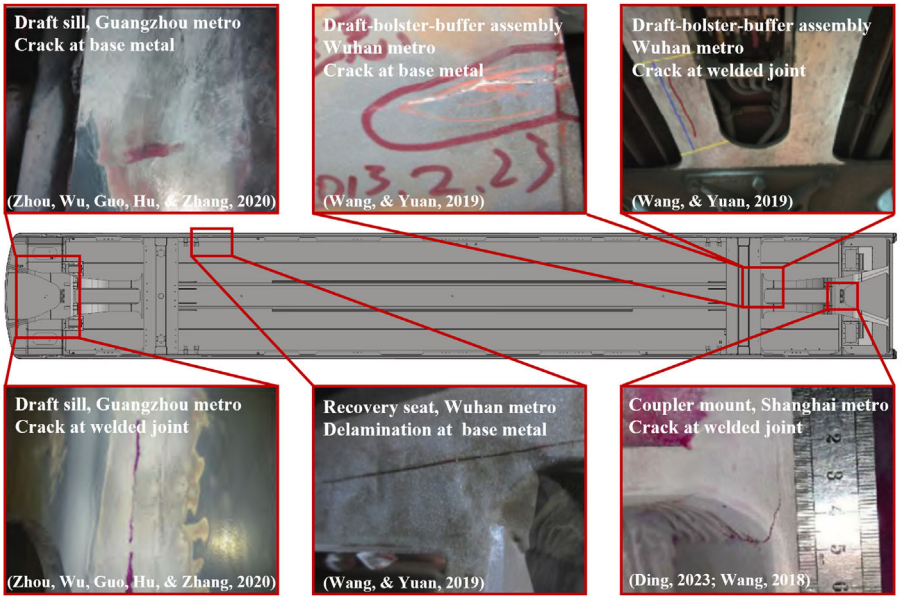

Source(s): Authors' own work

Figure 1.
Schematic diagram of typical defects on metro car bodies

However, the applications of aforementioned methodologies have not been extended to the car body of subway trains. As a pioneering development, Zeng, Jin, Zhu, Liu, and Zhang (2022), Zeng, Jin, He, Xiao, and Chen (2024) developed an entire life-cycle assessment framework specifically for the car body of electric locomotives. This framework incorporated the testing fatigue spectra with two estimation methods of the damage cumulative life and the residual life.

Subway trains exhibit distinctive operating characteristics from high-speed trains, high-speed maglev trains or electric locomotives. These include frequent traction/braking (Wu, Lu, Mou, Wang, & Liu, 2023), and a "tidal flow" pattern of asymmetric passengers (Li, Bai, Chen, Ming, & Cao, 2022) with the rush hour and holiday ridership significantly exceeding that of other periods. These distinct characteristics expose the metro car bodies to underestimated severe fatigue loads, potentially resulting in premature fatigue failure before designed life (Wang, Zhu, Yang, Xiao, & Yang, 2024; Jun, Kim, Kwon, Lee, & Seo, 2017).

Therefore, an in-depth investigation of the fatigue performance of a metro car body was dedicated in this study based on the operational loads. A comprehensive framework was established consisting of the field test, material property measurements, the fatigue strength verification based on the infinite life design principle, the service life estimation based on the safe life design principle, the residual life assessment based on the damage tolerance design principle. The ultimate aim is to provide theoretical insights and technical support for the structural enhancement and the maintenance decision.

2. Field test overview

The 2023 annual report of the Guangzhou Metro Co., Ltd. highlights an impressive average daily ridership of 8.6 million, outperforming all other urban railway systems in China. In particular, the Line 3 (including its branches) has distinguished itself with an average daily ridership of 1.8 million, thereby solidifying its reputation as the most trafficked subway line. It is reasonable to assume that the field test conducted on this line could provide a unique opportunity to evaluate the overloaded performance of the subway train and obtain service loads of the metro car body.

As shown in Figure 2, a six-vehicle formation of the B-type subway train was prepared for the field test. The train was designed to achieve a maximum speed of 120 km/h. Based on simulated results and maintenance records of similar subway platforms, strain gauges were strategically orientated at the critical locations that could exhibit high stress or prone to

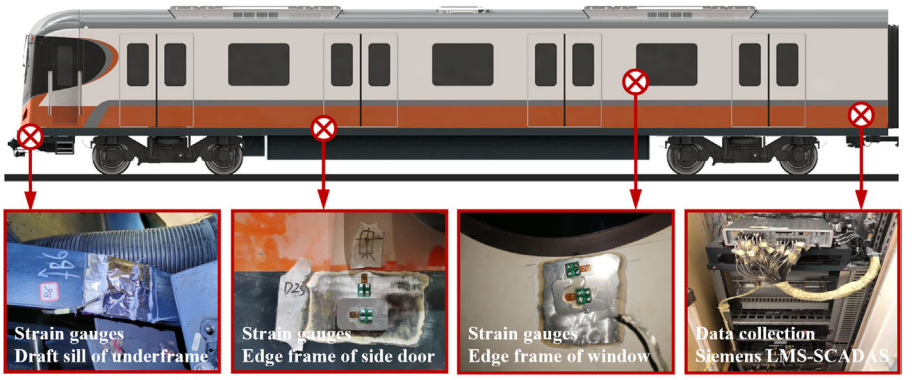

Figure 2.
Schematic diagram on field test of metro car bodies

Source(s): Authors' own work

damage. The sensitivity coefficient of these strain gauges is 2.17 ± 1%, and the semi-bridge circuit is used for the temperature compensation.

In addition, three-way acceleration (ACC) sensors with a sensitivity of 20.4 mV/(m/s^2) were installed at both ends and in the center of the underframe. Throughout the field test procedure, the subway train remained in regular service. Two sets of data collections were equipped on board to capture dynamic strain signals and acceleration histories from above-mentioned gauges and sensors. The range of these data collections is ±10000 με, ±10 V and 20–20000 Hz, while the corresponding sensitivity is ±0.5% FS, ±1% and ±0.1 dB. These test signals were recorded at a high sampling frequency of 1024 Hz and labelled on the daily basis. The field test duration included 34 weekdays, 12 weekend days and three public holidays to cover a representative sample of the tidal flow pattern of the passengers.

The primary test signals do not convey the immediacy of fatigue loads as effectively as the fatigue loading spectra. Although an exhaustive analysis of operational fatigue loading spectra has been presented in Section 4.2, for the sake of illustration, a segment of the stress signals on the reinforcing rib of bolster was thus depicted in Figure 3. These signals have been transformed through a series of data processes, such as filtering, denoising and the offset correction.

3. Fatigue strength verification

3.1 Standard fatigue loads

According to the principle of infinite life design, fatigue cracks will not originate in the defect-free structures when the extreme value of fluctuating stress is always maintained below the fatigue endurance limit during the service lifetime. In this sense, the anti-fatigue design issue can be simplified to a static strength verification problem in engineering applications.

Many design guidelines for the car body of rolling stocks have specified the methods of aforementioned fatigue strength verification and corresponding fatigue resistance design, including but not limited to UIC 566-1990, JIS E 7106-2018 and TB/T 3550.1-2019. These guidelines generally specify equivalent design loads for the fatigue strength verification. These loads are generally specified as an upper bound estimate of static forces and quasi-static accelerations, and thus are referred as standard design loads.

For instance, the metro car body in this study conformed to the standard EN 12663-2014, thus specified standard design loads include: longitudinal ACCs (±0.15 *g*), lateral ACCs (±0.15 *g*), vertical ACCs (0.85 *g* and 1.15 *g*), the traction effort F_{LT} (±36.7 kN per bogie) and the braking effort F_{LB} (±24.8 kN per bogie). A total of 24 cases were developed for the fatigue strength verification by considering the combination of these standard design loads. The detailed combination for each case can be found in the reference (Jin, Lu, Zhu, & Li, 2023).

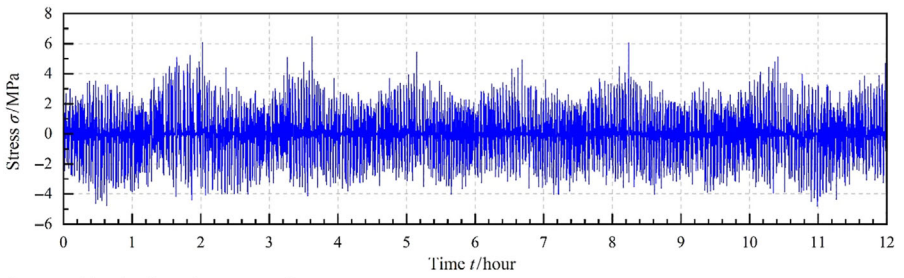

Source(s): Authors' own work

Figure 3.
Stress signal on reinforcing rib of bolster by field test

3.2 Finite element model

A fine Finite Element (FE) model containing 1.84 million elements and 1.61 million nodes was established to obtain the stress distribution of the metro car body in this study. As shown in Figure 4, a railway coordinate system was applied to the FE model with the positive direction of x-axis pointing to A-end of the vehicle, and the positive direction of y-axis pointing to A-side.

The primary skeleton of this metro car body was formed as an integral load-bearing structure welded by extruded Al alloys profiles of EN AW 6005A-T6 and a few Al alloys sheets of EN AW 6082-T6. In this FE model, these thin-shelled components were conducted by shell elements with a target element size of 15 mm. According to the standard EN 1999.1.1-2023, the Young's modulus of these Al alloys was set to 70 GPa, the Poisson's ratio was 0.3 and the unit mass was 2.70E−9 t/mm^3.

According to the standard EN 15663-2018, the design weight of the metro vehicle in working order status (AW0) is 20.671 t, and the design weight in the normal payload status (AW2) is 33.691 t. In the FE model, a few concentrated mass elements were adopted together with coupled rigid elements to simulate massive equipment, besides that, many dispersed mass elements were adhered to passenger spaces on the floor and corresponding installation areas to represent the mass of interior decorations, passengers and other equipment. The simulated results of the stress and the displacement by this FE model could be in a good agreement with the static bench test results of the metro car body.

3.3 Fatigue utilization factor

The DVS 1608-2011 standard, which is well-known and widely used in railway industry, defines a resultant fatigue utilization factor U_R for the fatigue verification, as shown in Equation (1). In accordance with this German guideline, the infinite fatigue life can be ensured when U_R is not greater than 1.0.

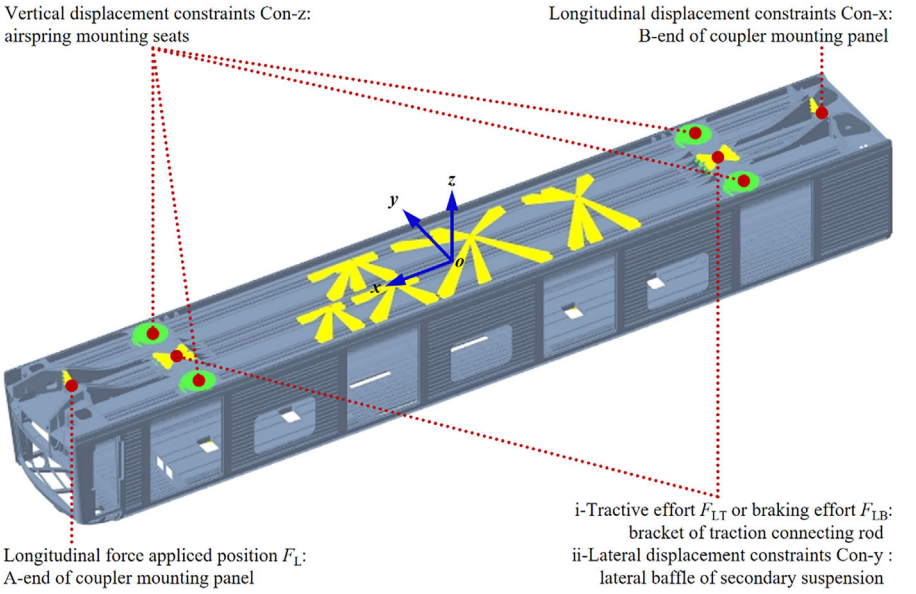

Figure 4.
Finite element model and boundary conditions

Source(s): Authors' own work

$$U_{\mathrm{R}} = \sqrt{U_{\sigma_1}^2 + U_{\sigma_2}^2 + U_{\tau}^2 + f_{\mathrm{V}} \cdot U_{\sigma_1} \cdot U_{\sigma_2}} \tag{1}$$

in which $U_{\sigma 1}$ and $U_{\sigma 2}$ are the fatigue utilization factor of the normal stress, U_{τ} is the fatigue utilization factor of the shear stress, $U_{\sigma 1}$, $U_{\sigma 2}$ and U_{τ} are defined as the ratio of normal stresses (σ_1 and σ_2) or the shear stress (τ) to the corresponding admissible limit (σ_{s} or τ_{s}), f_{V} is the influence coefficient of the normal stress σ_1 or σ_2.

The stress analysis was first performed based on the FE model and boundary conditions shown in Figure 4. Subsequently, the stresses in Base Metals (BMs) and Welded Joints (WJs) were resolved into the corresponding local coordinate systems of the respective FE elements. This process culminated in the determination of the maximum or minimum stress values over 24 simulated cases. As illustrated in Figure 5, the admissible limits of BMs and WJs were represented as the Moore–Kommers–Japer (MKJ) diagrams defined in the standard DVS 1608-2011.

The simulated results show that the U_{R} was less than 1.0 at all locations of the metro car body, indicating that the car body could meet the infinite life design principle. Figure 6 delineated top five locations with the most pronounced U_{R}, which were defined as the Fatigue Key Points (FKPs). Notably, the maximum U_{R} was 0.688, occurring at the edge frame of side window.

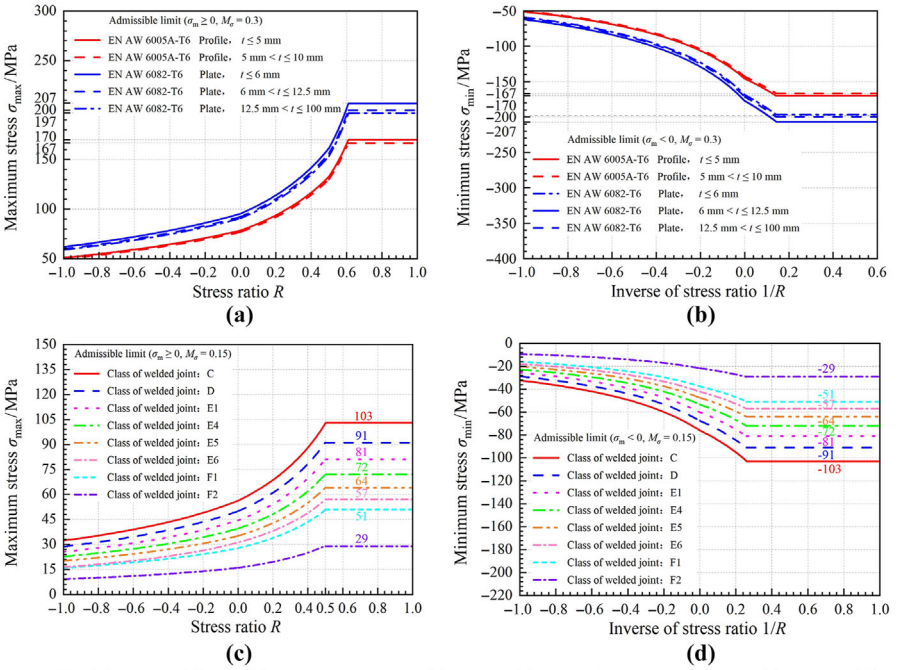

Figure 5.
MKJ diagrams of Al alloys 6005A and 6082 defined in DVS 1608-2011

Note(s): (a) BM with positive mean stress; (b) BM with negative mean stress; (c) WJs with positive mean stress; (d) WJs with negative mean stress

Source(s): Authors' own work

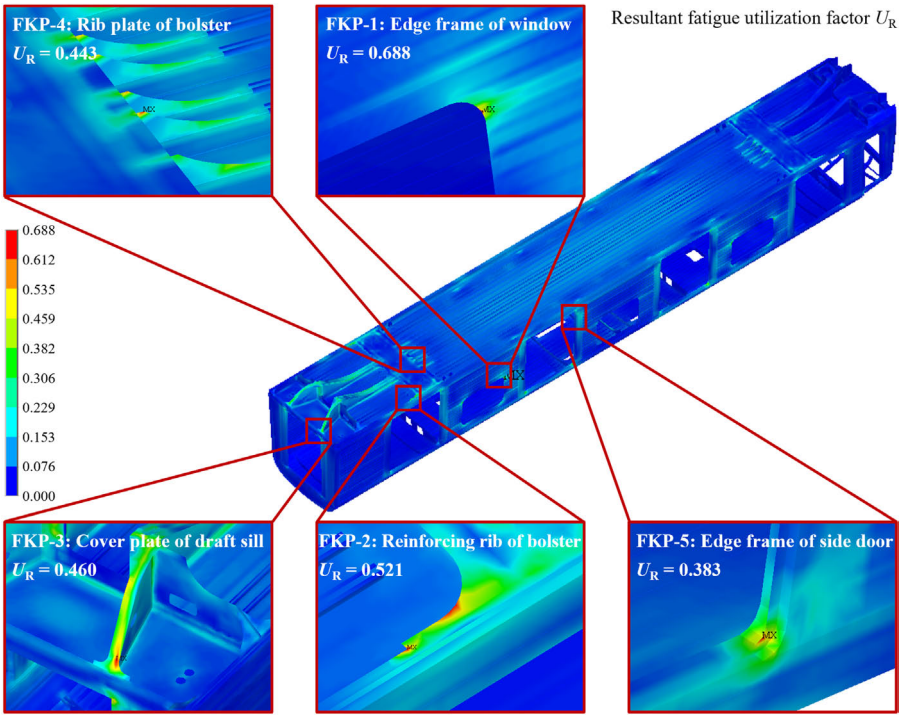

Figure 6.
Contour plot of resultant fatigue utilization

Source(s): Authors' own work

4. Service life estimation

4.1 High-cycle fatigue performance

Following the principle of fatigue damage accumulation, each fatigue cycle experienced by a structure is equivalent to a reduction in its fatigue resistance capacity. The structure succumbs to the fatigue failure when its fatigue resistance energy is completely exhausted. For engineering applications, the high-cycle fatigue curve, more formally known as the S–N curve, is widely used to quantify the fatigue resistance performance.

Many fatigue resistance design guidelines have provided high-cycle fatigue curves for various BMs and WJs of Al alloys, these S–N curves are typically defined by the classical Basquin equation or its modified forms. For engineering structures, such as subway trains subject to variable amplitude fatigue loads, these design guidelines generally recommend dual S–N curves with an endurance limit.

For instance, a standardized S–N curve defined in EN 1999.1.3-2023 for structures that subjected to variable amplitude fatigue loads is defined by a modified form of the Basquin equation, as shown in Equation (2) and Figure 7(a).

$$N = \begin{cases} N_C \times \left(\dfrac{\Delta\sigma_C}{\Delta\sigma}\right)^{m_1} & N \le N_D \\ N_D \times \left(\dfrac{\Delta\sigma_C}{\Delta\sigma}\right)^{m_2} \times \left(\dfrac{2}{5}\right)^{\frac{m_2}{m_1}} & N_D < N \le N_L \end{cases} \tag{2}$$

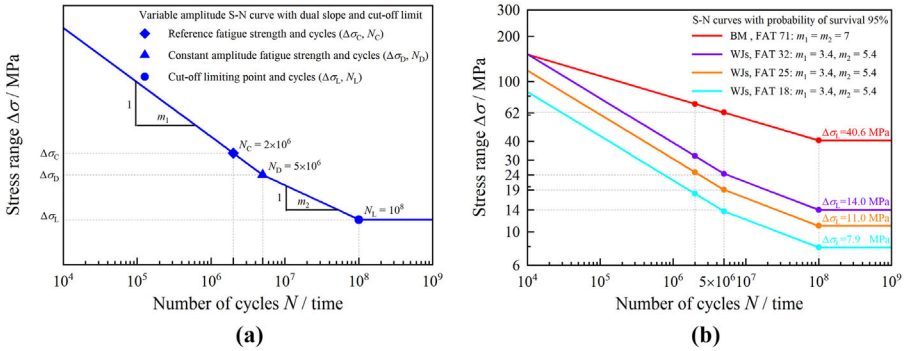

(a) **(b)**

Figure 7.
S–N curves of Al alloys for variable amplitude loads

Note(s): (a) Standardized S-N curve defined in EN 1999.1.3-2023; (b) S-N curves in log-log coordinates for detail categories of BM and WJs

Source(s): Authors' own work

in which N is the fatigue cycles, $\Delta\sigma$ is the stress range, m_1 and m_2 are the dual slopes, $N_C = 2 \times 10^6$, $N_D = 5 \times 10^6$ and $N_L = 10^8$ are fatigue cycles corresponding to the reference fatigue strength $\Delta\sigma_C$, constant amplitude fatigue limit $\Delta\sigma_D$, cut-off limit $\Delta\sigma_L$, respectively.

The reference fatigue strength $\Delta\sigma_C$ together with the dual slopes m_1 and m_2 are essential parameters required for the S–N curve as depicted in Figure 8(a) and Equation (2). These can be obtained from the detail categories defined in Annex J of EN 1999.1.3-2023. A total of five identified FKPs in Figure 6 were assigned to four Fatigue Classes (FATs) by matching the construction details, initiation sites and the stress orientations to the detail types of Annex J. The S–N curves of FAT 71, FAT 32, FAT 25 and FAT 18 were shown in Figure 7(b), where the reference fatigue strength $\Delta\sigma_C$ was equal to the FAT, the dual slopes of the BM were both 7.0 and the two slopes of WJs were 3.4 and 5.4, respectively.

4.2 Fatigue loading spectra

In this work, the field test signals were first reorganized to reflect the tidal flow pattern of passengers, and test data from one public holiday, two weekend days and four weekdays were carefully selected for the fatigue loading analysis. This selection covered a total operation millage of 5,578 km during a seven days' period. Selected stress histories were proportionally extrapolated to a design lifespan of 30 years, equivalent to 6.60 million km. These stress histories were compiled into fatigue loading spectra with 16 stress categories using a statistical method of rain-flow counting, the fatigue loading spectra of five FKPs identified in Figure 6 were shown in Figure 8.

All stress cycles below the cut-off limit $\Delta\sigma_L$, which is assumed to 10^8 cycles, can be considered as non-damaging. As shown in Figure 8(a)–(c), there are two stress categories of FKP-1, six stress categories of FKP-2 and five stress categories of FKP-4 above the cut-off limit $\Delta\sigma_L$. The fatigue life of these FKPs is no longer infinite, while all stress categories of FKP-3 and FKP-5 below the cut-off limit $\Delta\sigma_L$ have an infinite life, as shown in Figure 8(d).

4.3 Damage accumulation life

Based on Equation (2) and Miner damage cumulative law, the damage accumulation life of FKPs can be calculated by Equation (3). The damage accumulation life of five FKPs identified in Figure 6 were shown in Table 1.

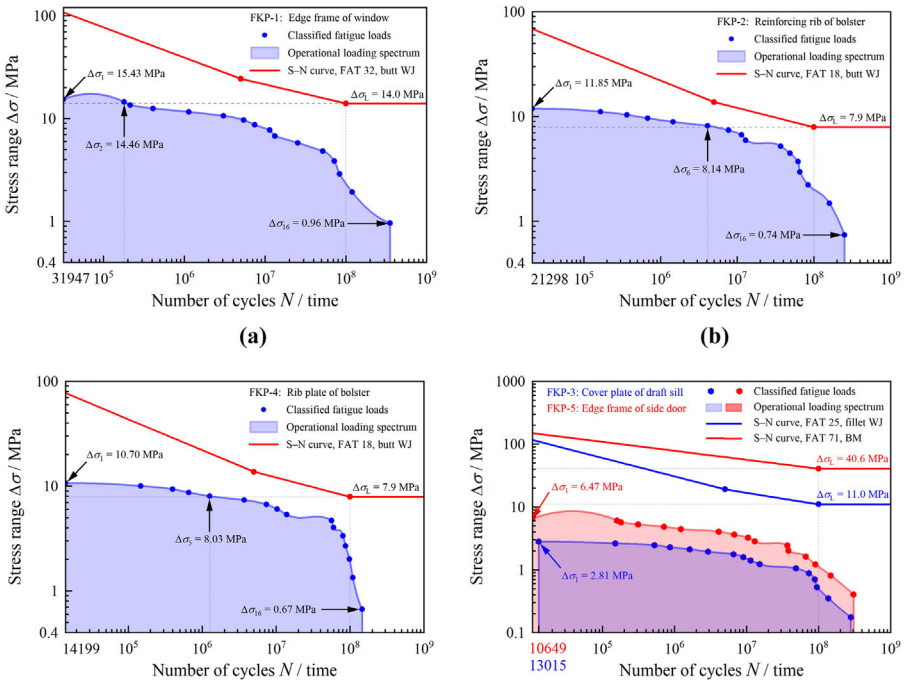

Figure 8.
Measured operational loading spectra from field test

Note(s): (a) FKP-1 edge flame of window; (b) FKP-2 reinforcing rib of bolster; (c) FKP-4 rib plate of bolster; (d) FKP-3 cover plate of draft sill and FKP-5 edge frame of side door
Source(s): Authors' own work

FKPs	Location	FAT	Damage	Damage accumulation life (10^6 km)
1	Edge frame of window	32	0.0074	891.89
2	Reinforcing rib of bolster	18	0.12	55.00
3	Cover plate of draft sill	25	0.00	Infinite
4	Rib plate of bolster	18	0.0037	1783.78
5	Edge frame of side door	71	0.00	Infinite

Table 1.
Damage accumulation life of FKPs based on operational loading spectra

Source(s): Authors' own work

$$L = L_S \Bigg/ \left[\sum_{\Delta\sigma_i \geq \Delta\sigma_D} \frac{n_i}{N_C \left(\frac{\Delta\sigma_C}{\gamma_{Mf} \cdot \gamma_{Ff} \cdot \Delta\sigma_i} \right)^{m_1}} + \sum_{\Delta\sigma_D < \Delta\sigma_i \leq \Delta\sigma_L} \frac{n_i}{N_D \left(\frac{\Delta\sigma_C}{\gamma_{Mf} \cdot \gamma_{Ff} \cdot \Delta\sigma_i} \right)^{m_2} \cdot \left(\frac{2}{5} \right)^{\frac{m_2}{m_1}}} \right] \tag{3}$$

in which L is the damage accumulation life, L_s is the fatigue life of loading spectra, $\Delta\sigma_i$ and n_i are the stress range and cycles of the ith of fatigue loading spectra, $\gamma_{Mf} = 1.1$ and $\gamma_{Ff} = 1.1$ are partial factors for the fatigue performance and fatigue loads.

It can be clearly found that the damage accumulation life of all FKPs significantly exceeds the design life of the metro car body. Nonetheless, when subjected to operational fatigue loads by the field test, No. 1, 2 and 4 of FKPs exhibit finite fatigue life. Interestingly, although the resultant fatigue utilization factor $U_R = 0.688$ of FKP-1 is higher than the $U_R = 0.521$ of FKP-2, the latter demonstrates a shorter fatigue life 55.00 million km than the former 891.89 million km. This discrepancy implies that FKP-2 is likely experiencing more pronounced dynamic influence than FKP-1.

5. Residual life assessment

5.1 Fracture resistance measurement

Considering unavoidable welded defects and potential service damage, it is very essential to perform a damage tolerance assessment procedure to further ensure the structural integrity and operational safety of the metro car body at the critical locations where significantly affected by dynamic operational loads, such as FKP-2.

Drawing upon the attributes of the WJ of FKP-2, a butt-welded plate of Al alloys 6005A was fabricated for the fracture resistance measurement. According to GB/T 21143-2014, three-point bending (3PB) specimens were cut from the butt-welded plate with an initial notch depth of 12 mm. Based on the K-decreasing method, a fatigue crack of 1.5 mm in length was first prefabricated, after which an extensometer was attached to perform the quasi-static loading test on these 3PB specimens, meticulously recording the applied force F and opening displacement of the crack mouth V. The F–V curves were plotted as depicted in Figure 9(a), and the test was ceased when a marked, sustained and uniform decreasing tendency was observed.

As shown in Figure 9(a), the maximum applied force F_{max} of these 3PB specimens were recorded in Table 2. The linear regression analysis was thus applied to fit the measured data with the linear F–V curves where the opening displacement of the crack mouth V was less than 0.1 mm. Subsequently, the slopes of fitted curves were biased by reducing by 5% of their original values. The intersection points of adjusted curves and the original curves were identified as the provisional force F_Q, and also recorded in Table 2. The provisional force F_Q of all 3PB specimens were less than the maximum applied force F_{max}, these data were valid.

Reference to GB/T 21143-2014, the provisional fracture toughness K_Q of 3PB specimens can be calculated by Equation (4) and Equation (5). According to GB/T 21143-2014, all of the calculated K_Q could simultaneously satisfy the dimensional criteria, the preliminary fatigue

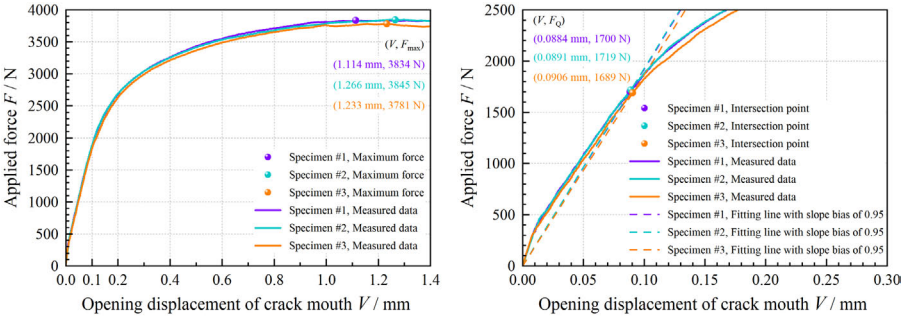

(a) **(b)**

Note(s): (a) Measured data; (b) Fitting data

Source(s): Authors' own work

Figure 9.
Fracture toughness properties of butt WJs of Al alloys 6005A

crack criteria and F–V curve criteria. Therefore, all of K_Q values recorded in Table 2 can be regarded as the indicative fracture toughness at the plan strain condition K_{IC}. The mean value of K_{IC} is 11.944 MPa$\sqrt{m}$ with a root mean square value of 0.366 MPa$\sqrt{m}$ which indicated a very small scatter between measured fracture toughness values of these 3PB specimens.

$$K_Q = f\left(\frac{a}{W}\right)\cdot\frac{S\cdot F_Q}{B\cdot W^{1.5}} \tag{4}$$

$$f\left(\frac{a}{W}\right) = \frac{3\left(\frac{a}{W}\right)^{0.5}\cdot\left[1.99-\left(\frac{a}{W}\right)\cdot\left(1-\frac{a}{W}\right)\cdot\left(2.15-\frac{3.93a}{W}+\frac{2.7a^2}{W^2}\right)\right]}{2\left(1+\frac{2a}{W}\right)\cdot\left(1-\frac{a}{W}\right)^{1.5}} \tag{5}$$

in which $a = 13.5$ mm is the depth of initial crack.

Adhering to the GB/T 6398-2017, several Compact Tensile (CT) specimens were cut from the center of the butt-welded plate with a width of 60 mm and a thickness of 12 mm. As shown in Figure 10(a), the prefabricated fatigue crack was parallel to the direction of the weld toe. These CT specimens were used for the crack growth rate test by the K-increasing method, where the applied constant amplitude load was 8,000 N with a stress ratio R of 0.1

Table 2. Dimensions of 3PB specimens and fracture toughness results

Specimen					Measurement		Calculation
No.	Thickness B (mm)	Width W (mm)	Span S (mm)	Length L (mm)	Maximum force F_{max} (N)	Provisional force F_Q (N)	Provisional fracture toughness K_Q (MPa$\sqrt{m}$)
1	12.12	23.98	96.00	112.83	3,834	1,700	11.926
2	12.11	23.90	96.00	112.91	3,845	1,719	12.211
3	12.12	24.07	96.00	112.54	3,781	1,689	11.694

Source(s): Authors' own work

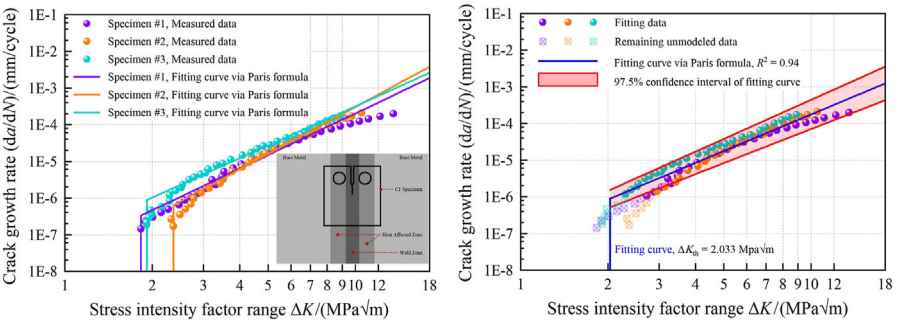

(a) **(b)**

Note(s): (a) Measured data in log-log coordinates; (b) Fitting curve in log-log coordinates

Source(s): Authors' own work

Figure 10. Crack growth relationships of butt WJs of Al alloys 6005A

and a frequency of 20 Hz. The crack growth rates of these CT specimens were measured by the flexibility method and plotted in Figure 10(a).

According to EN 1999.1.3-2023, crack growth rates of Al alloys could be defined by the Paris formula as Equation (6).The obtained threshold value of Stress Intensity Factor (SIF) ΔK_{th} was first obtained as: 1.826 MPa$\sqrt{m}$, 1.913 MPa$\sqrt{m}$ and 2.360MPa$\sqrt{m}$. The mean value of these ΔK_{th} is 2.033 MPa$\sqrt{m}$. As shown in Figure 10(b), the linear part of the measured data, where the crack growth rate was greater than 10^{-6} mm/cycle, was used to fit the Paris formula. Fitting parameters C and m of the mean fitting curve could be 3.319 and 7.072 with a well goodness of 0.94.

$$\frac{da}{dN} = C \cdot (\Delta K)^m \; \Delta K > \Delta K_{th} \tag{6}$$

in which ΔK is the range of SIF, ΔK_{th} is the threshold value of SIF, C and m are the fitting coefficient and index factor for the Paris formula.

It can be found from Figure 10(b) that at a confidence level of 97.5% the linear part of the measured data could be completely covered by the confidence interval. Following the principle of conservative assessment and design, the upper limit of this confidence interval with fitting parameters $C = 3.549$ and $m = 6.903$ were used in this work to assess the damage tolerance life.

5.2 Flaw tolerance dimension

As shown in Figure 11, typical flaws in similar structures with FKP-2 manifest as a through thickness crack originating at the end of WJ. The maximum depth of cracks ever detected was 11.0 mm. Based on the flaw regularization principle defined in BS 7910-2019, the reference failure plane of FKP-2 could be simplified to a rectangular plane with a width $W = 250$ mm and a thickness $B = 15$ mm. The crack progression direction was characterized from the end of the rib towards to the bolster.

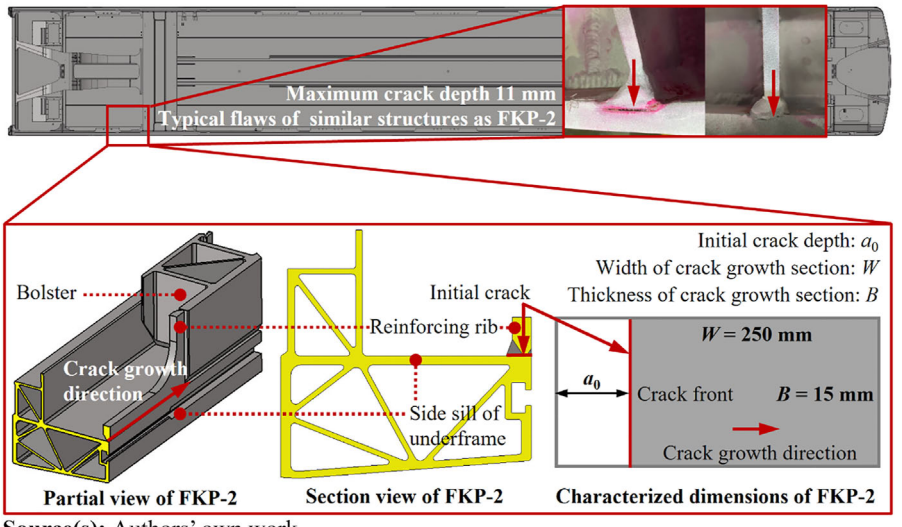

Source(s): Authors' own work

Figure 11.
Typical flaw and characterized dimensions of FKP-2

Based on the principle of residual strength design, the residual life of structures will be exhausted when the assessment point indicates a critical dimension of crack, lying beyond the safety region of the Fracture Assessment Diagram (FAD). According to the FAD Option 1 defined in BS 7910-2019, the failure assessment line can be constructed by Equation (7) and depicted in Figure 12(a).

$$\begin{cases} K_r = \left(0.3 + 0.7e^{-\mu L_r^6}\right) \cdot \left(1 + 0.5L_r^2\right)^{-0.5} & 0 < L_r \le 1 \\ K_r = [K_r(L_r = 1)] \cdot L_r^{\left(\frac{\varphi-1}{2\varphi}\right)} & 1 < L_r \le L_{max} \end{cases} \tag{7}$$

in which K_r is the fracture ratio, L_r is the load ratio, $L_{max} = 0.5\,[1+(\sigma_U/\sigma_Y)]$ is the maximum fracture ratio, $K_r\,(L_r = 1)$ is the fracture ratio when the load ratio $L_r = 1$. ϕ and μ are material parameters, in which $\phi = 0.3\,[1-(\sigma_U/\sigma_Y)]$, and μ is the lesser value between 0.001 (E/σ_Y) and 0.6.

Load ratio L_r is defined as the ratio of reference stress σ_{ref} to yield strength σ_Y, it can be calculated by Equation (8) from BS 7910-2019.

$$L_r = \frac{\sigma_{ref}}{\sigma_Y} = \frac{P_b + \sqrt{P_b^2 + 9P_m^2}}{3\sigma_Y \cdot \left(1 - \frac{a}{W}\right)} \tag{8}$$

in which P_b and P_m are the bending stress and membrane stress of the reference failure plane, respectively.

For the field test was conducted under the AW0 status, the bending stress $P_b = 4.30$ MPa and membrane stress $P_m = 11.23$ MPa of FKP-2 were first calculated by the FE model shown in Figure 4. Subsequently, the maximum tensile stress value of 7.05 MPa was obtained in the fatigue loading spectra. Following the principle of conservative assessment and design, these two stresses were summarized to be the high valuation of the membrane stress P_m. Therefore, the membrane stress P_m and bending stress P_b in Equation (8) could be 18.28 MPa and 4.30 MPa, respectively.

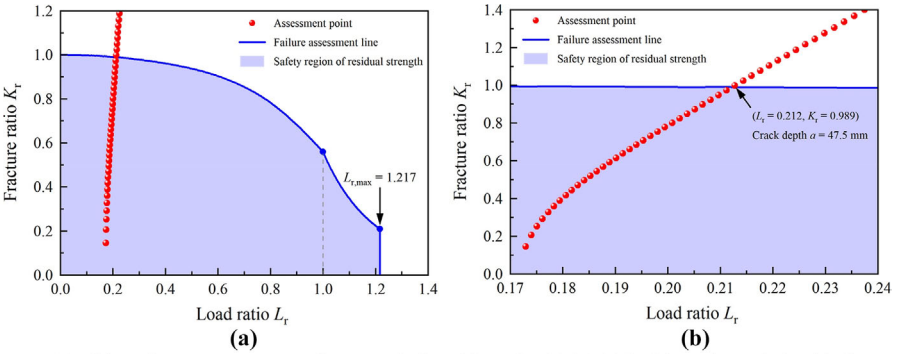

Figure 12.
Failure assessment diagram of FKP-2

Note(s): (a) Failure assessment diagram defined in BS 7910-2019; (b) Enlarged detail view
Source(s): Authors' own work

Fracture ratio K_r is defined as the ratio of SIF K to fracture toughness K_{IC}, it can be calculated by Equation (9) and Equation (10) from BS 7910-2019.

$$K_r = \frac{K}{K_{IC}} = \frac{Y \cdot (P_b + P_m) \cdot \sqrt{\pi \cdot a}}{K_{IC}} \tag{9}$$

$$Y = 1.12 - 0.23 \cdot \left(\frac{a}{W}\right) + 10.6 \cdot \left(\frac{a}{W}\right)^2 - 21.7 \cdot \left(\frac{a}{W}\right)^3 + 30.4 \cdot \left(\frac{a}{W}\right)^4 \tag{10}$$

in which Y is the correction factor for SIF, it is defined by Equation (10).

As shown in Figure 12(b), when the crack depth a = 47.5 mm, the corresponding assessment point first lied beyond the safety region of the FAD, considering about a flow detection accuracy of 0.5 mm in the railway vehicle engineering, thus the flaw tolerance dimension was determined to be 47.0 mm.

5.3 Damage tolerance life

Reference to BS 7910-2019, the fatigue loading spectra of stress range and corresponding cycles in Section 4.2 could be transformed to fatigue loading spectra of SIF range and corresponding cycles by Equation (10) and Equation (11).

$$\Delta K_i = Y \cdot \Delta\sigma_i \cdot \sqrt{\pi \cdot a} \tag{11}$$

Since the stress range on the first category of the fatigue loading spectra for FKP-2 was 11.85 MPa, an initial crack depth a_0 = 7.5 mm could be calculated by Equation (11) when the SIF range ΔK was equal to the threshold SIF ΔK_{th} = 2.033 MPa$\sqrt{m}$. Therefore, if the initial crack depth a_0 was less than 7.5 mm, the residual life of FKP-2 was infinite.

A similar assessment method was implemented to conditions that the initial crack depth was greater than 7.5 mm. The damage tolerance life in years was equal to the crack growth life when the crack propagated from an initial depth 7.5 mm–47.0 mm. These assessment results were shown in Figure 13(a).

As shown in Figure 13(a), the damage tolerance life of FKP-2 will significantly diminish with the increase of initial crack depth. If the linear coordinates of Figure 13(a) were transformed into the log-log coordinates of Figure 13(b), the damage tolerance life of FKP-2 could be clearly delineated into three stages: an initial slow propagation stage, when 7.5 mm ≤ a_0 ≤ 10.0 mm;

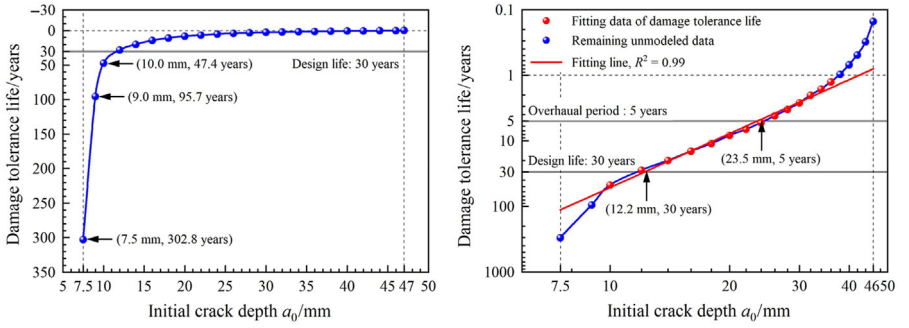

Note(s): (a) Assessment results; (b) Fitting line in log-log coordinates

Source(s): Authors' own work

Figure 13.
Damage tolerance life of FKP-2

followed by a steady propagation stage, when 10.0 mm < $a_0 \leq$ 36.0 mm; culminated in a rapidly propagation stage, when 36.0 mm < a_0 < 47.0 mm.

During the steady propagation stage, the damage tolerance life of FKP-2 exhibited a well linear pattern. Therefore, a damage tolerance life assessment formula with a very well goodness of 0.99 was thus constructed by the linear regression analysis method as Equation (12) and plotted in Figure 13(b).

$$\log(L) = 4.443 - 2.731 \cdot \log(a_0)\ 10.0\,\text{mm} \leq a_0 \leq 36.0\ \text{mm} \tag{12}$$

Figure 13(b) revealed that Equation (12) could provide a rather conservative damage tolerance assessment result at the initial propagation stage while it was not conservative in the rapidly propagation stage. Fortunately, the damage tolerance life at the rapidly propagation stage was significantly less critical compared to the other stages in the engineering realm, such as railway vehicles. This is because, from the operation safety, it is quite challenging to make the decision to allow the subway train remaining in service when the damage tolerance life of the metro car body was less than one year.

Equation (12) could thus be a pivotal tool in enhancing the design and dictating maintenance decisions. For instance, it indicates that even with an initial crack depth of 12.2 mm at FKP-2, the damage tolerance life can still be aligned with the intended 30-year design lifespan. Historical data reveals that the maximum crack depth detected in analogous structures is a mere 11.0 mm, underscoring the robust of the fatigue resistance capability of FKP-2. Nonetheless, it is strongly advocated to implement a high-quality sealing weld at the fabrication stage for end locations analogous to FKP-2. This preemptive measure is proposed as the most straightforward and cost-effective strategy to counteract the initiation and progression of cracks, thereby ensuring the longevity and reliability of FKP-2 and the similar structures.

Based on Equation (12), the damage tolerance life of FKP-2 is adequate to encompass an overhaul period of five years when the crack depth does not exceed 23.5 mm. This criterion can serve as a benchmark for damage tolerance-based maintenance strategies. Assuming the precondition information is sufficiently reliable, the maintenance frequency for metro car bodies can be appropriately reduced. Such an economical maintenance strategy can lead to a reduction in operational costs and an enhancement in operational efficiency.

6. Conclusions

A field test was first conducted on a heavily trafficked metro line to accurately determine and analyze the service loads experienced by the car body of a B-type metro train. Subsequently, the fracture properties of a butt-welded joint were characterized through the fracture toughness and crack propagation tests which were applicable to fatigue prediction and structural integrity assessment. The fatigue resistance of the metro car body was verified by the fatigue utilization factor, employing standard fatigue loads from EN 12663-2014 and in accordance with MKJ diagrams from DVS 1608-2011. The top five locations with the most significant fatigue utilization factors were recognized as FKPs. The damage accumulation life of these FKPs was estimated using S–N curves defined in EN 1999.1.3-2023, alongside the fatigue loading spectra derived from the field test data.

Maintenance records from analogous subway platforms indicated that through thickness cracks originating at the end of the reinforcing rib were the typical defect at FKP-2. The flaw tolerance dimension at FKP-2 was estimated using the FAD defined in BS 7910-2019, in conjunction with the measured and fitted fracture toughness. The damage tolerance life of FKP-2 was assessed using the SIF calculation equation defined in BS 7910-2019, operational fatigue loading spectra, and the crack growth rate obtained and fitted by test. Finally, an

empirical equation was thus proposed to evaluate the damage tolerance life for any detected cracks and determining the maximum tolerable depth for a specified service duration. From foregoing studies, the following conclusions can be drawn as:

(1) The metro car body exhibited a maximum fatigue utilization factor of 0.688 at FKP-1, while the maximum cumulative damage of the metro car body was 0.12 at FKP-2, neither of which exceeded the threshold of 1.0. These metrics indicate that the metro car body is capable of an intended design life of 30 years or an operational distance of 6.6 million km, thereby fulfilling the design life requirement.

(2) The cumulative damage of FKP-1, FKP-2 and FKP-4 has exceeded than 0.0, with the minimum damage tolerance life of 55.0 million kilometers, which reveals the influence of dynamic fatigue loads by the field test was significant. This finding indicated that the single fatigue strength verification with the standard fatigue loads could not achieve the design objective of infinite life. It is recommended that both service life estimation and residual life assessment are integrated into the framework of fatigue life assessment to further ensure the operational safety of the metro car body.

(3) The maximum damage tolerance depth of FKP-2 was 47.0 mm, and the crack threshold depth was 7.5 mm. For a projected design life of 30 years, the flow tolerance depth was 12.2 mm, and even with a crack depth of 23.5 mm had been detected, the residual life of FKP-2 could still cover an overhaul period of five years. These results underline the robust defect tolerance capability of FKP-2.

In this study, the field test and the structural integrity principle have been introduced to the classical fatigue assessment framework, thereby the influence of operational loads and defects can be taken into account for the fatigue research of metro car body. Notably, this framework presented here still requires additional refinement. For instance, as reported by Mann, Härkegård, and Stärk (2007), the short crack growth rate of Al alloys 6082-T6 will increase with the mean tensile stress, the influence of mean stress on crack growth rates merits further investigation, particularly in the context of variable amplitude fatigue loading conditions. It is thus recommended that fatigue growth tests should be conducted under a range of stress ratio, along with the development of three-parameter fatigue loading spectra that consider mean stress, stress range and cycles. These recommendations may enhance the accuracy of fatigue life predictions for metro car bodies.

References

Ding, Y. Q. (2023). Management and control strategy of urban rail transit vehicle car body cracks based on safety risk assessment. *Urban Mass Transit*, *26*(6), 301–305.

Guo, F., Wu, S. C., Liu, J. X., Wu, Z. K., Fu, S. Q., & Ding, S. S. (2021). A time-domain stepwise fatigue assessment to bridge small-scale fracture mechanics with large-scale system dynamics for high-speed maglev lightweight bogies. *Engineering Fracture Mechanics*, *248*, 107711. doi: 10.1016/j.engfracmech.2021.107711.

Guo, F., Hu, F. F., Wu, S. C., He, F., Liu, J. X., & Wu, X. W. (2022). System dynamics in structural strength and vibration fatigue life assessment of the swing bar for high-speed train. *International Journal of Mechanical System Dynamics*, *2*(2), 178–189. doi: 10.1002/msd2.12045.

Guo, F., Wu, S. C., Liu, J. X., Wu, X. W., & Zhang, W. H. (2023). An innovative stepwise time-domain fatigue methodology to integrate damage tolerance into system dynamics. *Vehicle System Dynamics*, *61*(2), 550–572. doi: 10.1080/00423114.2022.2051567.

Hu, F. F., Wu, S. C., Xin, X., Guo, F., & Ren, Z. S. (2023). Determination of the critical defect and fatigue life of high-speed railway axles under variable amplitude loads. *International Journal of Fatigue*, *168*, 107446. doi: 10.1016/j.ijfatigue.2022.107446.

Jin, X. H., Lu, J., Zhu, Y., & Li, X. T. (2023). Optimization of simulation analysis method for car body structural strength. *Electric Locomotives and Mass Transit Vehicles*, *46*(5), 1–7.

Jun, H. K., Kim, J. C., Kwon, S. J., Lee, D. H., & Seo, J. W. (2017). Fatigue crack analysis in a bolster of a metro strain. *Engineering Failure Analysis*, *76*, 44–54. doi: 10.1016/j.engfailanal.2017.02.005.

Li, Z. R., Bai, Y., Chen, Y., Ming, X. J., & Cao, Y. W. (2022). Optimization model of unpaired timetable for metro train under asymmetric passenger flow. *China Railway Science*, *43*(6), 207–218.

Lu, Y., Li, S., & Shen, T. L. (2022). Analysis and repair of cracks in drag box of the aluminum alloy metro vehicles body. *Mechanical and Electrical Engineering Technology*, *51*(12), 301–305.

Mann, T., Härkegård, G., & Stärk, K. (2007). Short fatigue crack growth in aluminium alloy 6082-T6. *International Journal of Fatigue*, *29*(9-11), 1820–1826. doi: 10.1016/j.ijfatigue.2007.01.002.

Wang, S. H. (2018). Analysis of causes to cracking in carbodies of trains for Shanghai Rail Traffic No.1 Line and measures for solution. *Rolling Stock*, *56*(3), 41–43.

Wang, F. Q., & Yuan, S. R. (2019). Draft, Bolster and buffer assembly crack repairing and post-evaluation of Al-alloy body for metro vehicle. *Railway Locomotive and Car*, *39*(S0), 80–85.

Wang, C., Zhu, T., Yang, B., Xiao, S. N., & Yang, G. W. (2024). Failure analysis of stress corrosion cracking in welded structures of aluminum alloy metro body traction beam in service. *Engineering Failure Analysis*, *163*(Part B), 108564. doi: 10.1016/j.engfailanal.2024.108564.

Wu, S. C., Ren, X. Y., Kang, G. Z., Ma, L. J., Zhang, X. J., Qian, K. C., & Teng, W. X. (2021). Progress and challenge on fatigue resistance assessment of railway vehicle components. *Journal of Traffic and Transportation Engineering*, *21*(1), 81–114.

Wu, Y. F., Lu, Y. J., Mou, R., Wang, L., & Liu, X. (2023). A study on optimization of staring strategy for metro trains based on traction and braking characteristics. *Electric Drive for Locomotives*, *6*, 99–105.

Zeng, Y. J., Jin, X. H., He, Y. Q., Xiao, Q., & Chen, D. Y. (2024). Damage characteristics and residual life evaluation of heavy-duty electric locomotive body based on measured stress spectrum. *Railway Locomotive and Car*, *44*(3), 84–90.

Zeng, Y. J., Jin, X. H., Zhu, T., Liu, H. Y., & Zhang, H. H. (2022). Life-cycle assessment method for key parts of an electric locomotive body. *Electric Drive for Locomotives*, *6*, 10–16.

Zhou, X. R., Wu, S. C., Guo, F., Hu, Y. N., & Zhang, X. J. (2020). Typical defects and remanufacturing & repairing technologies of modern railway vehicle components. *Electric Welding Machine*, *50*(9), 31–35.

Corresponding author
Feng Guo can be contacted at: gfnz9@163.com, 010200002366@crrcgc.cc